



Article

IONORING: Real-Time Monitoring of the Total Electron Content over Italy

Claudio Cesaroni ^{1,*} , Luca Spogli ^{1,2} and Giorgiana De Franceschi ¹

¹ Istituto Nazionale di Geofisica e Vulcanologia, 00143 Rome, Italy; luca.spogli@ingv.it (L.S.); giorgiana.defranceschi@ingv.it (G.D.F.)

² SpacEarth Technology, 00143 Rome, Italy

* Correspondence: claudio.cesaroni@ingv.it

Abstract: IONORING (IONospheric RING) is a tool capable to provide the real-time monitoring and modeling of the ionospheric Total Electron Content (TEC) over Italy, in the latitudinal and longitudinal ranges of 35°N–48°N and 5°E–20°E, respectively. IONORING exploits the Global Navigation Satellite System (GNSS) data acquired by the RING (Rete Integrata Nazionale GNSS) network, managed by the Istituto Nazionale di Geofisica e Vulcanologia (INGV). The system provides TEC real-time maps with a very fine spatial resolution (0.1° latitude x 0.1° longitude), with a refresh time of 10 min and a typical latency below the minute. The TEC estimated at the ionospheric piercing points from about 40 RING stations, equally distributed over the Italian territory, are interpolated using locally (weighted) regression scatter plot smoothing (LOWESS). The validation is performed by comparing the IONORING TEC maps (in real-time) with independent products: (i) the Global Ionospheric Maps (GIM) - final product- provided by the International GNSS Service (IGS), and (ii) the European TEC maps from the Royal Observatory of Belgium. The validation results are satisfactory in terms of Root Mean Square Error (RMSE) between 2 and 3 TECu for both comparisons. The potential of IONORING in depicting the TEC daily and seasonal variations is analyzed over 3 years, from May 2017 to April 2020, as well as its capability to account for the effect of the disturbed geospace on the ionosphere at mid-latitudes. The IONORING response to the X9.3 flare event of September 2017 highlights a sudden TEC increase over Italy of about 20%, with a small, expected dependence on the latitude, i.e., on the distance from the subsolar point. Subsequent large regional TEC variations were observed in response to related follow-on geomagnetic storms. This storm is also used as a case event to demonstrate the potential of IONORING in improving the accuracy of the GNSS Single Point Positioning. By processing data in kinematic mode and by using the Klobuchar as the model to provide the ionospheric correction, the resulting Horizontal Positioning Error is 4.3 m, lowering to, 3.84 m when GIM maps are used. If IONORING maps are used as the reference ionosphere, the error is as low as 2.5 m. Real-time application and services in which IONORING is currently integrated are also described in the conclusive remarks.

Keywords: TEC maps; single point positioning; ionosphere; space weather; mid-latitude ionosphere



Citation: Cesaroni, C.; Spogli, L.; De Franceschi, G. IONORING: Real-Time Monitoring of the Total Electron Content over Italy. *Remote Sens.* **2021**, *13*, 3290. <https://doi.org/10.3390/rs13163290>

Academic Editor: Yunbin Yuan

Received: 14 July 2021

Accepted: 18 August 2021

Published: 19 August 2021

Publisher's Note: MDPI stays neutral with regard to jurisdictional claims in published maps and institutional affiliations.



Copyright: © 2021 by the authors. Licensee MDPI, Basel, Switzerland. This article is an open access article distributed under the terms and conditions of the Creative Commons Attribution (CC BY) license (<https://creativecommons.org/licenses/by/4.0/>).

1. Introduction

The ability to monitor and model the environmental conditions in near-Earth space is of paramount importance for modern technological infrastructures vulnerable to a variety of electromagnetic phenomena of differing spatial and temporal scales, usually originating on the Sun and disrupting the near-Earth space environment via magnetosphere-ionosphere coupling [1]. These phenomena are included in the so-called “Space Weather”. Particularly sensitive to the geospace conditions is the ionosphere at high and low latitudes with the formation of electron density irregularities of different scale sizes (from hundreds of km down to cm) affecting radio waves crossing them (see, e.g., [2–4]).

The mid-latitude ionosphere may also be a theatre of serious disturbing phenomena propagating from the higher latitudes and combining with the equatorial ionosphere

reaction to space weather events, e.g., the super fountain phenomenon, for which the crests of the Equatorial Ionospheric Anomaly, where daily irregularities are more likely to occur, migrate to higher latitudes (see, e.g., [5–7]). The disturbed electric field named Prompt Penetration Electric Fields (PPEFs) and the Storm-time Equatorward Winds (SEW) are responsible for the creation of this super fountain effect [8,9]. Space Weather Impacts on the ionosphere at mid-latitudes include the occurrence of traveling ionospheric disturbances (TID), i.e., wave-like disturbances in ionospheric electron density. Large-scale traveling ionospheric disturbances (LSTIDs) have been observed using different instruments [10] and are usually attributed to traveling atmospheric disturbances (TADs) produced by the Joule and particle heating triggered by the magnetospheric energy deposited in the auroral oval during the storm [11]. Cesaroni et al. 2017 [12] speculate that the wave-like electron density and airglow observed at mid-latitudes, in Southern Italy, could be a consequence of a poleward expansion of the northern crest of the Equatorial Ionization Anomaly (EIA). The enhanced airglow propagating from the north and the electron density waves resulted from energy injected at auroral latitudes as confirmed by magnetometer observations in Scandinavia.

From the complex scenario here briefly outlined, it can be easily argued the need for ionosphere monitoring and modeling on a global and regional scale, especially to support, in real-time, GNSS (Global Navigation Satellite System)-based services becoming increasingly demanding in terms of accuracy that may be seriously compromised by the ionosphere, the larger source of the errors induced on GNSS signals (see e.g., [13–15]). On the other hand, GNSS signals are useful probes for the investigation of the distribution of the free electrons in the ionosphere [16]. Given the dispersive nature of the plasma, it is possible to derive the Total Electron Content (TEC) from GNSS multi-frequency receivers. TEC is the integral of electron density along the path satellite-receiver at ground, usually measured in TEC units (TECU), corresponding to 10^{16} electrons/m². Nowadays, the availability of dense networks of GNSS receivers facilitates the use of TEC data for mapping and modeling the ionosphere at different spatial and temporal scales, to aid services development for different classes of end-users.

From a global perspective, the International GNSS Service (IGS) releases highly valuable vertical TEC Global Ionospheric Maps (GIM) in the form of different products (rapid and final products, <https://www.igs.org/products> accessed on 17 August 2021), with variable latency. GIMs are based on the joint efforts for GNSS data processing by the IGS ionospheric working group (Iono-WG), available online since 1998 [17], and are tested by comparison with external data [18] and with TEC combined products provided by different centers. Using ionospheric data streams based on the Radio Technical Commission for Maritime Services (RTCM) standard provided by the Chinese Academy of Science, the Centre National d'Etudes Spatiales, and the Universitat Politècnica de Catalunya, the IGS combined real-time-GIM has been generated and validated in real-time conditions. Zishen Li et al., 2020 [19] emphasized the need for the multi-layer ionospheric assumption in the presence of large latitudinal gradients to reach the goal of real-time TEC mapping. Still, within the global ionosphere, recent efforts have been addressed to the establishment of an ionosphere mapping service that would combine measurements from two independent sensor networks: IGS permanent GNSS receivers and ionosondes of the Global Ionosphere Radio Observatory (GIRO, [20]), providing the bottom-side electron density profiles. Global average (climate) maps of TEC are introduced and used with the slab thickness based on the climatological capabilities of the IRI (International Reference Ionosphere) model [21], with the aim at supporting the future development, at a global scale, of the actual ionosphere state in real-time [22].

For what concerns the regional TEC monitoring and mapping, since 2012 the Royal Observatory of Belgium (ROB) provides TEC maps over Europe, making use of the dense Regional Reference Frame Sub-Commission for Europe (EUREF) permanent GNSS network [23]. ROB-TEC maps are delivered in near real-time with a latency of about 3 min, refresh time of 15 min, and a spatial resolution of 0.5° latitude × 0.5° longitude. The ROB

software system comprises a method that is able to de-correlate the estimation of the Differential Code Biases (DCBs) and slant TEC (sTEC) in order to follow the ionospheric disturbances in near real-time. The ROB system has been tested with good results against IGS-GIM products and during several Space Weather events, including the Halloween storm which occurred in 2003 [23].

TEC maps over China and adjacent areas have been generated by using GNSS data from IGS and CMONOC (Crustal Movement Observation Network of China) networks and adopting a data assimilation method based on the Kalman filter [24]. The study highlighted the improvements that can be achieved by data assimilation in providing TEC maps over China with a spatial and temporal resolution of 1° latitude \times 1° longitude \times 5 min, respectively. Mendoza et al., 2019 [25] developed a near real-time TEC mapping over Central and South America, the Caribbean, and the Antarctic Peninsula, with a latency of about 10 min and a spatial resolution of 0.5° latitude \times 0.5° longitude. The system uses GNSS data from BKG (Germany), IBGE (Brazil), IGN (Argentina), IGS, NASA (USA), SGM (Uruguay), UNAVCO (USA) showing a great collaborative effort for the common goal of the near real-time TEC mapping.

Opperman et al., 2007 [26] tested the possibility to adopt the adjusted spherical cap harmonic analysis for TEC mapping over South Africa. The method was developed in the 1990s for mapping the critical frequency of the ionospheric F2 layer from ionosonde data over Europe [27,28]. Opperman and co-authors used TEC data from the Chief Directorate Surveys and Mapping (CDSM), which operated a network of 40 geodetic dual-frequency Global Positioning System (GPS) receivers, and ionosonde data for comparison. They concluded that the method, suitably optimized, could be applied for near real-time TEC mapping over South Africa. Recently, the spherical cap harmonic analysis has been applied over Australia for the near real-time mapping and modeling of TEC, provided by the Australian Regional GPS Network (ARGN). The model makes use of an artificial neural network (ANN) to generate TEC values to fill the grid where experimental data are not available [29]. The model is able to map the TEC over Australia with a Root Mean Square Error (RMSE) of 2–3 TECU and is capable of reproducing its seasonal and hourly features.

This paper deals with the real-time monitoring and modeling of TEC over Italy that extends over a geographic area between mid-high latitude (48° N) to mid-low latitude (35° N) in a quite confined range of longitude centered at 12° E. The very fine spatial resolution ($0.1^\circ \times 0.1^\circ$ latitude, longitude) gives the opportunity to reproduce the ionosphere dynamics under quiet and disturbed conditions as well as its diurnal, seasonal, and solar flux-related variability. In Section 2, the data provided by the dense RING network and the approach adopted to calibrate TEC are detailed. Section 3 deals with the validation of the IONORING real-time product against TEC from GIMs (global and final products) and ROB maps (Europe, real-time product). The performance of IONORING is then evaluated in Section 4, by analyzing the TEC diurnal, seasonal, solar cycle, and latitudinal variations between 2017 and 2020, including also the response to the space weather disturbances that occurred in early September 2017. As a further demonstration of the potential of IONORING, Section 4 also contains an example of how IONORING can support ionospheric error mitigation in GNSS single-frequency positioning. Conclusions are given in Section 5, where the potential of IONORING to support science and end-user services is also highlighted.

2. Data and Method

Ionospheric RING (IONORING) leverages the data provided by the Rete Integrata Nazionale GNSS (RING, <http://ring.gm.ingv.it/>, accessed on 12 July 2021) (INGV RING working group, 2016) owned by the Istituto Nazionale di Geofisica e Vulcanologia. RING represents an important geodetic research infrastructure consisting currently of a distributed network over the Italian territory of more than 200 GNSS sensors (black circles in Figure 1). Almost all the stations are in the free field, thanks to the low-power consumption of the satellite transmission that can be run with solar panels. This significantly reduces the multipath-related errors in the GNSS observables. All the stations are equipped with

a professional GPS receiver and a choke ring antenna. These features make the RING receivers particularly suitable for ionospheric studies, as also demonstrated in the recent literature [12,30,31]. Among all the RING receivers, some have been selected to feed IONORING algorithm, by considering the trade-off between a homogenous coverage of the ionospheric sector and a minimum latency of the IONORING products availability. In order to cover the westernmost part of the considered region, the receivers in Ajaccio and Cagliari (red-dotted blue circles in Figure 1) managed by IGS are also included. In Figure 1, the receivers located in Montereale (*mter*, 42.51°N 13.21°E, green dotted) and in INGV headquarter (*ingr*, 41.83°N 12.51°E) are also reported. They are not included in IONORING, but used for validation and positioning application purposes, as described later in the text.

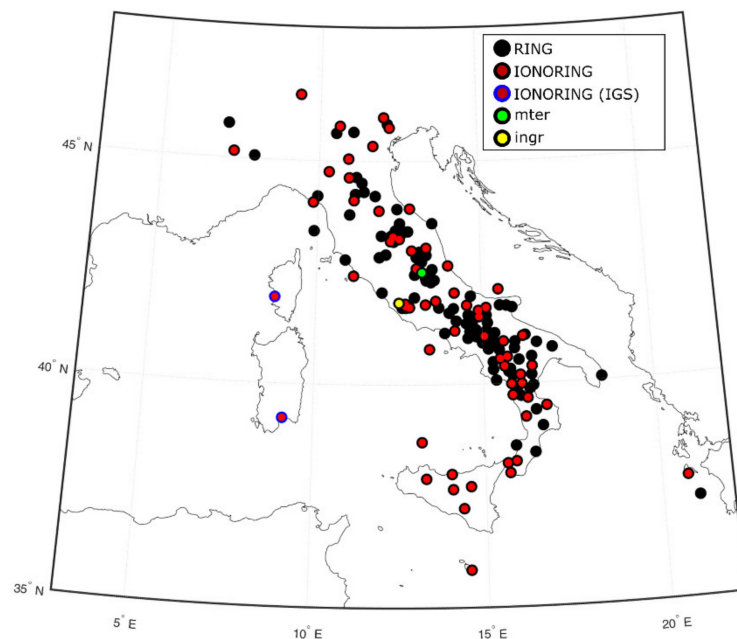


Figure 1. GPS receivers in RING (black circles) and in IGS (blue circles) networks; GPS receivers used for IONORING (red dotted); GPS receivers in Montereale (*mter*, 42.51°N 13.21°E, green dotted) and in INGV headquarter (*ingr*, 41.83°N 12.51°E), used for validation and positioning application purposes, respectively.

IONORING input data are GPS carrier phase observables on L1 and L2 frequencies (1575.42 MHz and 1227.60 MHz, respectively), Clear Acquisition (CA) code observables on L1, and Y-code observables on L2 that are broadcasted at a 1-second rate through Networked Transport of RTCM via Internet Protocol (NTRIP) by the selected receivers (red dots in Figure 1). Additionally, navigational information (i.e., orbital parameters for GPS satellites) are retrieved by NTRIP streaming from the considered receivers or, alternatively, by the IGS navigational information streaming.

From code and phase observables on L1 and L2 frequencies, we derive ionospheric sTEC, that is the integrated electron density along the ray-path connecting satellite and receiver. This is based on the fact that the ionospheric effects on GNSS signal propagation include range delay, being proportional to sTEC according to the following formula:

$$I[\text{TECu}] = \alpha \frac{\text{sTEC}}{f^2} \quad (1)$$

where sTEC is expressed in TEC units (TECu, 1 TECu = 10^{16} electrons/m²), I is the ionosphere-induced delay in length unit, and α is a conversion factor to obtain length units

from TECu. Thus, the TEC retrieval is obtained by calculating the geometry-free linear combination, that is defined as

$$\begin{aligned} L_{12_arc}[m] &= L_1 - L_2 \\ &= I_1 - I_2 + c(\tau_{1,R} - \tau_{2,R}) + c(\tau_{1,S} - \tau_{2,S}) + \lambda_1 N_1 + \lambda_2 N_2 + \varepsilon \end{aligned} \quad (2)$$

where subscripts 1 and 2 refer to L1 and L2 GPS frequencies, respectively, while λ refers to the corresponding wavelength, N is the ambiguity on carrier phase measurements, "arc" refers to continuous carrier phase observations (i.e., for which the product λN can be considered constant), τ is the frequency-dependent delay induced by the receiver (R) and satellite (S) hardware, c is the speed of light in vacuum, and ε is the noise in length units on the carrier phase observation combination.

From Equations (1) and (2), the following can be derived:

$$L_{arc}[TECu] = sTEC + B_R + B_S + C_{arc} + \varepsilon_L \quad (3)$$

where $B_R = c(\tau_{1,R} - \tau_{2,R})\frac{f^2}{\alpha}$ and $B_S = c(\tau_{1,S} - \tau_{2,S})\frac{f^2}{\alpha}$ are the so-called "inter-frequency biases" (IFBs) for carrier phase observations related to the receiver and the transmitter, respectively, $C_{arc} = \frac{f^2}{\alpha}(\lambda_1 N_1 + \lambda_2 N_2)$ is the ambiguity for the $L_1 - L_2$ combination and $\varepsilon_L = \frac{f^2}{\alpha}\varepsilon$ is the carrier phase noise in TECu.

Analogously, the geometry-free linear combination of the code measurements can be obtained as:

$$P [TECu] = sTEC + b_R + b_S + \varepsilon_P \quad (4)$$

where b_R and b_S are the corresponding IFBs, often called "differential code biases" (DCBs), due to the receiving and the transmitting hardware, and ε_P is the noise on code measurements. We let the reader notice that in Equation (4) there is not the ambiguity term present in Equation (2).

For every continuous arc of observations, by subtracting the two new observables (one for code measurements and the other one for phase measurements), the average difference between carrier phase and code observables along a single arc can be obtained:

$$\langle L_{arc} - P \rangle_{arc} = C_{arc} + B_R + B_S - b_R - b_S - \langle \varepsilon_P \rangle_{arc} \quad (5)$$

in which the noise associated with the phase measurements is neglected [Braasch, 1996].

By subtracting Equation (5) from (3), the following can be obtained:

$$\tilde{L}_{arc} = sTEC + b_R + b_S + \langle \varepsilon_P \rangle_{arc} \quad (6)$$

being the carrier-phase ionospheric observable leveled to the code-delay ionospheric observable. The term $\langle \varepsilon_P \rangle_{arc}$ is the effect of the noise and the multipath along the arc on carrier-phase observations, as described in Ciralo et al., 2007 [32]. One possible approach to estimate sTEC without neglecting $\langle \varepsilon_P \rangle_{arc}$ consists in evaluating a single bias for each arc, instead of different biases for receiver and satellite. Thus, Equation (6) can be written as:

$$\tilde{L}_{arc} = sTEC + \beta_{arc} \quad (7)$$

where β_{arc} is the sum of receiver and satellite biases ($b_R + b_S$) and multipath and other errors with non-zero mean. This is the equation from which a calibrated TEC can be obtained, by using the method described by Ciralo et al., 2007 [32]. Hereafter, we refer to this method as the "Gg calibration technique", or simply "Gg technique". In the specific, sTEC values are mapped as a two-dimensional surface by means of the classical thin shell method as

$$sTEC = vTEC(\phi_1, \phi_2) \cdot \sec \chi \quad (8)$$

where $vTEC(\phi_1, \phi_2)$ is the unknown describing a surface in the reference frame defined by a couple (ϕ_1, ϕ_2) over the thin shell (bi-dimensional) and χ is the angle formed by the

ray-path and the perpendicular to the shell at the ionospheric pierce point (IPP) [33,34]. In the case of the Gg technique, the reference frame is local time (LT) and modified dip latitude (Modip) proposed by Rawer et al., 1981 [35]. Then, the vTEC is expanded as a polynomial linear in LT and of the fourth-order in Modip. As a consequence, Equation (8) can be written as a linear relationship:

$$\tilde{L}_{\text{arc}} = \sec \chi \sum_n c_n p_n(\text{LT}, \text{Modip}) + \beta_{\text{arc}} \quad (9)$$

where p_n is the term of the polynomial and c_n the corresponding coefficient. Equation (9) can be solved via the standard least squares method.

Although this calibration technique is robust and widely used, especially for mid-latitude and low-latitude studies [12,36–41], it has the intrinsic limitation of not being operating in real-time. This is because it assumes the availability of complete arcs of observations. To overcome this limitation and for the purposes of the real-time operation of IONORING, we evaluate β_{arc} for each station-satellite couple and for a given day by computing its mean value on the previous 3 days.

The algorithm for β_{arc} calculation is here summarized:

1. Download of RINEX files for all the GNSS stations for the previous 3 days;
2. Evaluation of β_{arc} for each satellite-receiver pair for the previous 3 days by applying Gg calibration technique;
3. Calculation of the mean value over the previous 3 days for each satellite-receiver pair ($\hat{\beta}_{\text{arc}}$);
4. Creation of a lookup table containing $m \times n \hat{\beta}_{\text{arc}}$ values, being m the total number of RING stations, n the total number of operating GPS satellites.

The algorithm is run daily so that the lookup table is updated every 24 h. Previous studies have shown that the receiver and satellite DCBs variations between consecutive days are smaller than 0.5 ns (<1 TECu) for GPS satellites and smaller than 1 ns (<2 TECu) for the GPS stations (see, e.g., [42]). This allows considering β_{arc} as stable within 24 h. Assuming $\hat{\beta}_{\text{arc}} = b_R + b_S$, Equation (4) can be rewritten as:

$$sTEC = P - \hat{\beta}_{\text{arc}} - \varepsilon_P \quad (10)$$

in which the only remaining unknown is ε_P .

As per Equation (8), the values of vTEC are obtained by projecting sTEC to the vertical at the IPP and by considering the shell height at 350 km. The IPP coordinates are calculated in the WGS84 reference frame by using the positions of the receivers (derived from RINEX files) and of the satellites. The latter are evaluated by leveraging on the navigation information broadcasted by each receiver in its NTRIP streaming or alternately, from the IGS navigational information streaming.

To produce a vTEC map in which the impact of ε_P is mitigated, vTEC values estimated at every IPP from all considered satellite-receiver pairs are interpolated through a non-parametric local regression technique named LOWESS [43], which is an interpolation method that includes local data in the computation of the smoothing curve. LOWESS has been proven to be effective for regional TEC mapping purposes (see, e.g., [38]). The interpolation algorithm is first applied on the whole vTEC dataset to identify and reject outliers defined as:

$$\left| \widetilde{vTEC}(\phi_1, \phi_2) - vTEC(\phi_1, \phi_2) \right| > 2 RMSE \quad (11)$$

where $\widetilde{vTEC}(\phi_1, \phi_2)$ is the value of the smoothed vTEC curve evaluated at the IPP, identified by its coordinates (ϕ_1, ϕ_2) , while $vTEC(\phi_1, \phi_2)$ is the actual vTEC at the IPP and RMSE indicates the root mean square error of the dataset. After the outlier rejection, the LOWESS interpolation is reapplied on the clean dataset to provide the final vTEC map that is provided in terms of the smoothed vTEC curve evaluated on a regular grid of 0.1° latitude

$\times 0.1^\circ$ longitude that covers the geographical extent of $[35^\circ\text{N}, 48^\circ\text{N}]$ latitude and $[5^\circ\text{E}, 20^\circ\text{E}]$ longitude. The average latency of the full processing chain is less than a minute.

3. Results

To validate IONORING, we compare the vTEC maps with three independent products by considering 3 years of accumulated data covering the period 1 May 2017 to 30 April 2020. The products are: (i) the vTEC derived from the Montereale (*mter*, 42.51°N 13.21°E , not included in IONORING) receiver (green dot in Figure 1) by applying the Gg calibration technique (post-processing) and described in Section 2; (ii) the vTEC maps over Europe provided by ROB and available at <ftp://gnss.oma.be> (accessed on 17 August 2021) [23] and (iii) the GIMs provided as final combined solution product (“igsg”) by the IGS and available at <cddis.gsfc.nasa.gov> (accessed on 17 August 2021) [17].

Figure 2 reports the results of the comparison between vTEC over *mter* derived through the Gg calibration technique and vTEC from IONORING calculated at *mter* coordinates (42.51°N , 13.21°E). Panel a reports IONORING vTEC as a function of Gg vTEC. The linear fit (red-dashed line) and its features (see the textbox) are reported and the blue line indicates the bisector. Panel b reports the time profile of the difference between IONORING and Gg vTEC. Panel c shows the probability distribution of the difference between IONORING and Gg vTEC and the corresponding Gaussian fit (red), whose expression and parameters are also reported in the textbox. Panel d and e depict the hourly and monthly differences between IONORING and Gg vTEC, respectively. In the boxplots, the red line indicates the median, and the bottom and top edges of the box indicate the 25th and 75th percentiles, respectively, while the range marked by the dashed lines indicates the extrema.

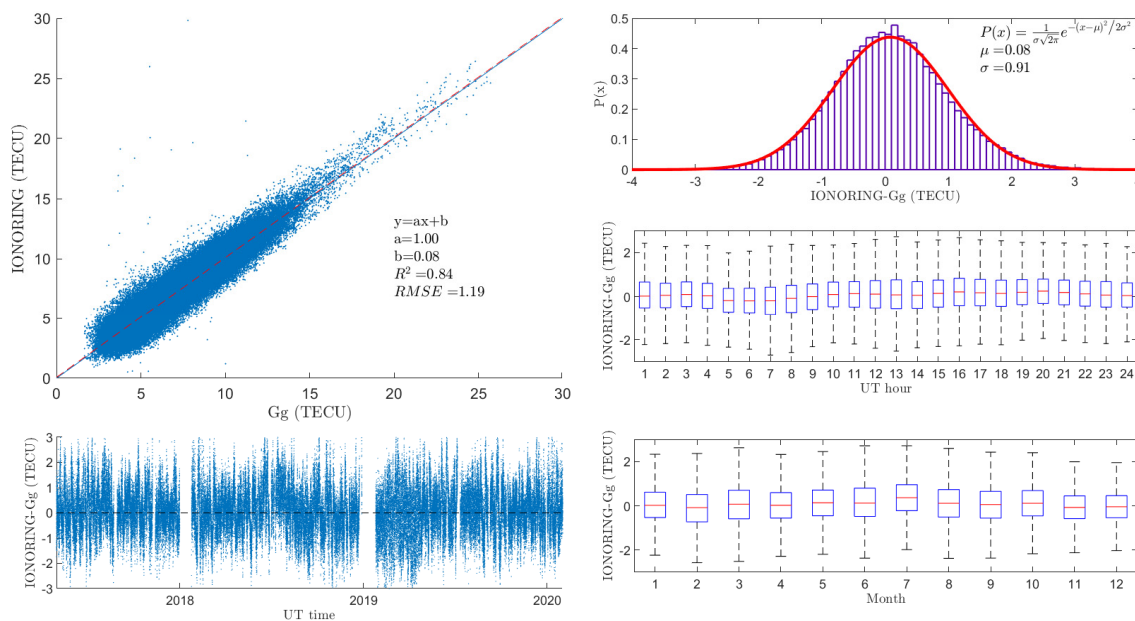


Figure 2. Scatter plot of vTEC from IONORING over *mter* against vTEC directly measured by *mter* and calibrated with Gg technique. The linear fit (red-dashed line) and its features (in the textbox) are reported, while the blue line indicates the bisector (panel a). Time profile of the difference between IONORING and Gg vTEC (panel b). Probability distribution of the difference between IONORING and Gg vTEC and the corresponding Gaussian fit (red), whose expression and parameters are also reported in the textbox (panel c). Boxplots of the hourly (panel d) and monthly (panel e) differences between IONORING and Gg vTEC. In the boxplots, the red line indicates the median, and the bottom and top edges of the box indicate the 25th and 75th percentiles, respectively, while the range marked by the dashed lines indicates the extrema.

By using the same representations of Figure 2, Figure 3 reports the results of the comparison between vTEC from ROB maps and vTEC from IONORING. The ROB maps are provided in the range [35°N, 62°N] latitude and [15°W, 25° E] longitude, with a spatial resolution of 0.5° and every 15 min with a latency of about 3 min [23]. For the comparison, we consider, for each time step, the average vTEC calculated over the entire IONORING map and the average vTEC calculated by limiting the ROB maps in the same geographical range of IONORING. Due to the different time resolutions, both IONORING and ROB maps are down-sampled at 30 min time resolution.

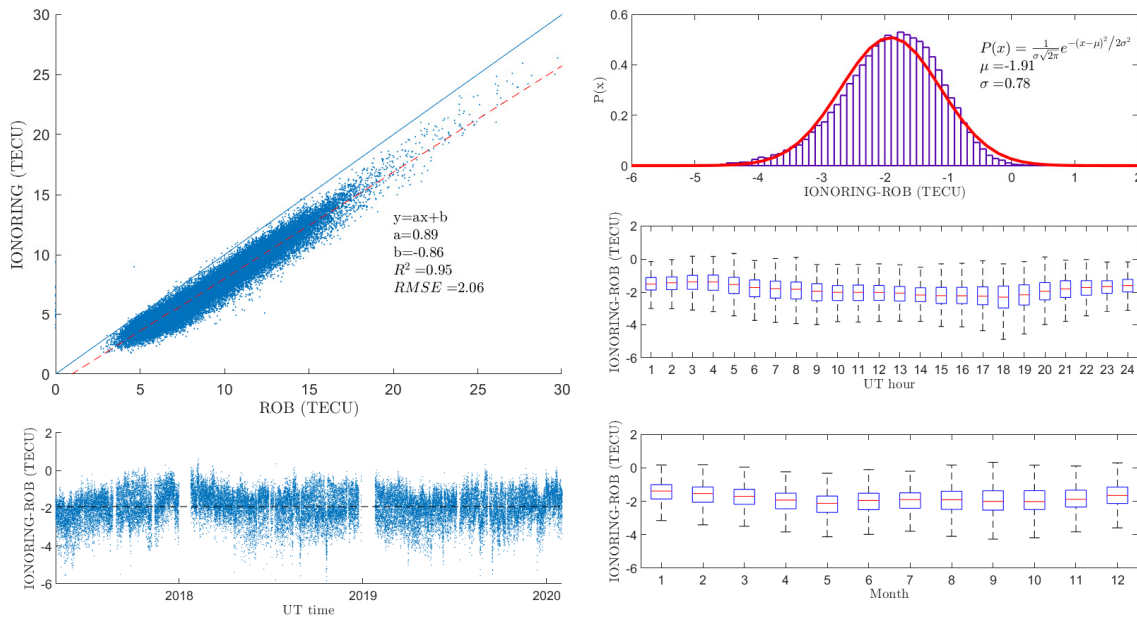


Figure 3. The same as Figure 2 but referring to the IONORING validation against the vTEC maps provided by the Royal Observatory of Belgium (ROB). The linear fit (red-dashed line) and its features (in the textbox) are reported, while the blue line indicates the bisector (panel a). Time profile of the difference between IONORING and ROB vTEC (panel b). Probability distribution of the difference between IONORING and ROB vTEC and the corresponding Gaussian fit (red), whose expression and parameters are also reported in the textbox (panel c). Boxplots of the hourly (panel d) and monthly (panel e) differences between IONORING and ROB vTEC. In the boxplots, the red line indicates the median, and the bottom and top edges of the box indicate the 25th and 75th percentiles, respectively, while the range marked by the dashed lines indicates the extrema.

By following the same approach adopted to compare with ROB maps, Figure 4 reports the results of the comparison between vTEC from IGS maps and vTEC from IONORING. The IGS GIM maps (final combined solution, “igsg”) are provided at a global level with a spatial resolution of 2.5° latitude x 5° longitude and every 2 h with a latency of about 11 days [17]. For this comparison, IONORING maps have been down-sampled to 2 h.

The summary of the validation results is reported in Table 1, in which the following parameters are provided: the angular coefficient (a), intercept (b) and coefficient of determination (R^2) of the linear regression (panels a of Figures 2–4), the RMSE of the vTEC differences, defined as:

$$RMSE = \sqrt{\frac{\sum_{i=1}^N (vTEC_{IONORING}^i - vTEC_{REF}^i)^2}{N}} \quad (12)$$

where $vTEC_{IONORING}^i$ is the IONORING vTEC at the time t_i and $vTEC_{REF}^i$ is the vTEC at the time t_i of reference products (REF= Gg, ROB, IGS), as described above. In addition, Table 1 reports the mean (μ) and the standard deviation (σ) of the Gaussian fit on the difference $vTEC_{IONORING}^i - vTEC_{REF}^i$ distribution reported in panels c of Figures 2–4. We

remind here again that data from *mter* are not included in IONORING maps and that vTEC over such receiver is retrieved by applying the Gg calibration technique as it is (i.e., in post-processing). Thus, the fit of the comparison with IONORING vTEC over the *mter* location, featured by $a = 1$, $b \sim 0$, reveals: (i) the goodness of the LOWESS interpolation method and (ii) the validity of the assumption that DCBs variability over 24 h is negligible. It is also worth noticing that the differences have no dependence on the year, time of the day, and season (panels b, d, and e of Figure 2, respectively).

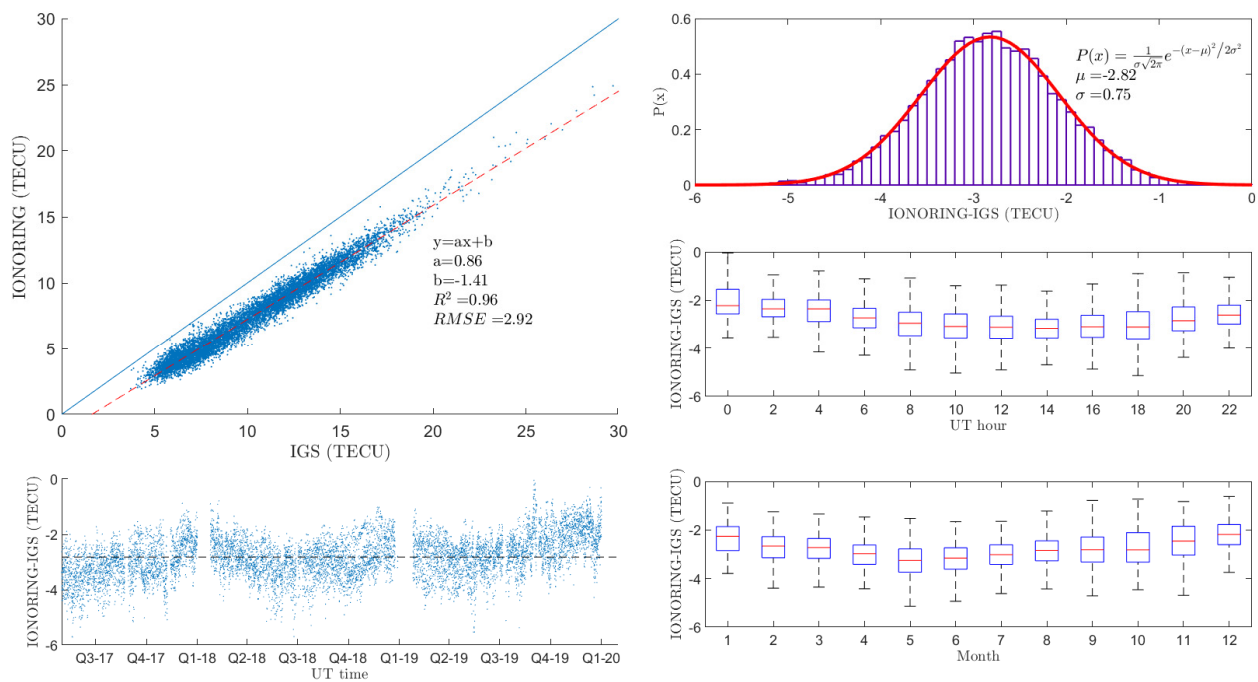


Figure 4. The same as Figure 2 but referring to the IONORING validation against the Global Ionospheric Maps (final products) provided by the International GNSS Service (IGS). The linear fit (red-dashed line) and its features (in the textbox) are reported, while the blue line indicates the bisector (panel a). Time profile of the difference between IONORING and IGS vTEC (panel b). Probability distribution of the difference between IONORING and IGS vTEC and the corresponding Gaussian fit (red), whose expression and parameters are also reported in the textbox (panel c). Boxplots of the hourly (panel d) and monthly (panel e) differences between IONORING and IGS vTEC. In the boxplots, the red line indicates the median, and the bottom and top edges of the box indicate the 25th and 75th percentiles, respectively, while the range marked by the dashed lines indicates the extrema.

Table 1. Summary table of the validation results.

Validation Dataset	a	b (TECu)	R^2	RMSE (TECu)	μ (TECu)	σ (TECu)
Gg	1.00	0.08	0.84	1.2	0.1	0.9
ROB	0.89	-0.86	0.95	2.0	-1.9	0.8
IGS	0.86	-1.41	0.96	2.9	-2.8	0.8

Concerning the comparison with ROB and IGS datasets, the coefficient of determination suggests an almost ideal correlation ($R^2 = 0.95$ and $R^2 = 0.96$, respectively). However, a mean difference of -1.9 ± 0.8 TECu with the ROB dataset and -2.8 ± 0.8 TECu with the IGS dataset is present.

To provide a qualitative comparison with other similar regional TEC products, far from being exhaustive, Figure 5 reports the RMSE resulting from the validation of IONORING against ROB and IGS maps (red) and that referred to different regional or local TEC products reported in selected recent literature. Even if a direct comparison among different

techniques is out of the scope of this paper, the aim of this figure is to illustrate how the difference of IONORING with the validation datasets is in agreement with what was reported by other authors, validating independent regional TEC mapping techniques. It is worth mentioning that the RMSE values reported in the literature are obtained by considering different inhomogeneous datasets, covering different ionospheric sectors, seasons, and helio-geophysical conditions.

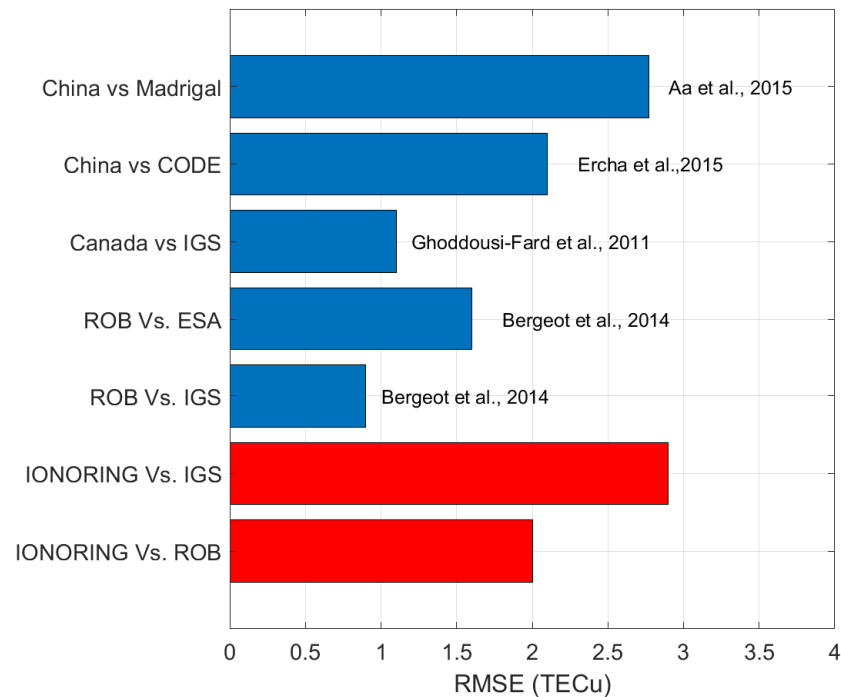


Figure 5. Root Mean Square Error resulting from the validation of different TEC mapping techniques. In red, the results reported in this paper (Figures 3 and 4).

4. Discussion

The performance of IONORING has been evaluated by characterizing the daily, seasonal, and latitudinal variations [44] in the same period considered for the validation (1 May 2017 to 30 April 2020). Additionally, the storm-time behavior [45] is also investigated, by considering the geomagnetic events that occurred in September 2017.

4.1. Seasonal, Daily and Latitudinal Variations

Figure 6 reports the daily variation of the mean v TEC for Italian low (37°N , blue), mid (42°N , orange) and high (47°N , yellow) latitudes (longitude is 12°E) for the period 1 May 2017 to 30 April 2020. The error bars represent the $\pm 1\sigma$ spread around the mean. As expected, the higher the latitude, the lower the TEC, as the latitudinal dependence of the ionization is dependent on the solar zenith angle. It is interesting to note how the peak TEC for low-latitude is at 12:00–13:00 UT (13:00–14:00 LT), while for mid- and high-latitudes it is at 11:00 UT (12:00 LT). This may be due to the fact that the Italian low-latitudes are sensitive to the effect of the increase of ionization in correspondence with the expected position of the northern crest of the EIA. In fact, while at mid-latitudes and at F2-layer peak heights the ionization is strongly driven by the zenith angle that peaks at noon [46], at low-latitudes the EIA is formed mainly from the removal of plasma from around the equator by the upward $\mathbf{E} \times \mathbf{B}$ drift [8], whose peak is expected at 14:00 LT [47], i.e., at a later time with respect to the local noon.

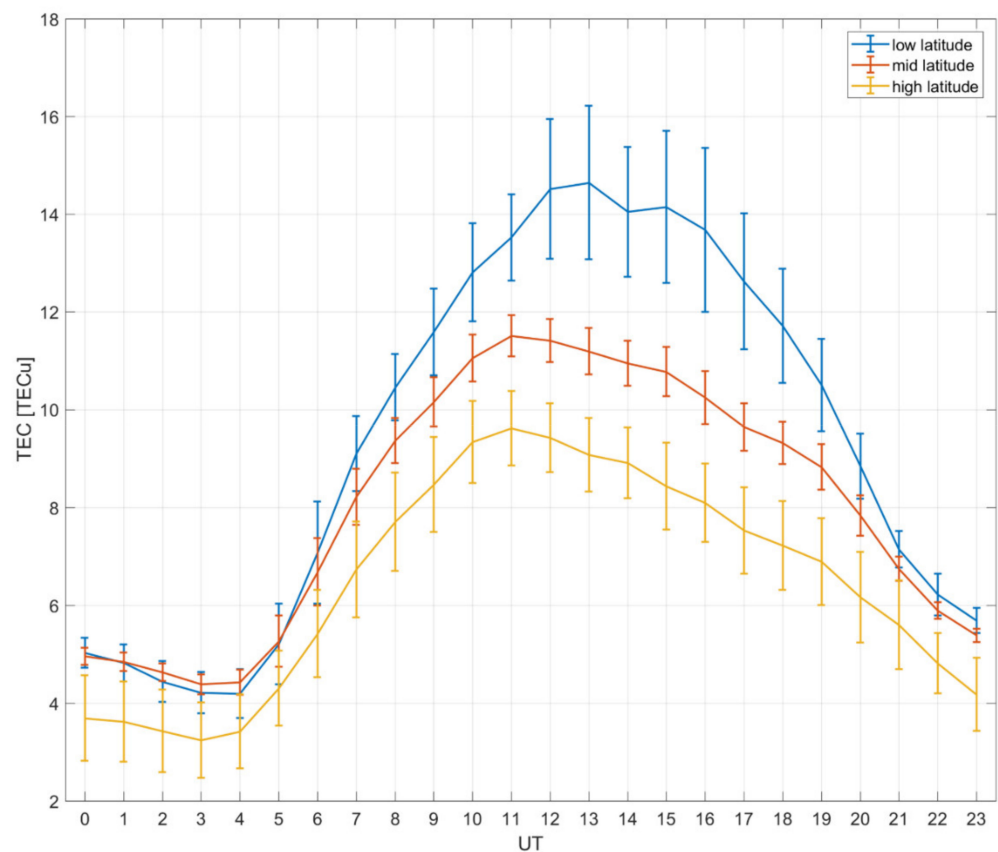


Figure 6. Mean daily variation of the TEC for Italian low (blue), mid (orange) and high (yellow) latitudes for the period 1 May 2017 to 30 April 2020. The error bars represent the TEC standard deviation.

To better characterize the average daily v TEC variation provided by IONORING, Figure 7 shows the maps of mean TEC at 00:00 UT (panel a), 06:00 UT (panel b), 12:00 UT (panel c), and 18:00 UT (panel d) by considering the period 1 May 2017 to 30 April 2020. From the Figure 7, it is possible to appreciate the less structuring of the ionosphere during the night-time (panel a), with the v TEC almost homogeneous at all latitudes, while at UT noon (panel c) the latitudinal dependence is stronger, smoothly decaying from lower to higher latitudes.

Figure 8 reports the seasonal variation of TEC over Italy obtained by considering the mean v TEC over the IONORING maps (black dots), evaluated every 10 min, in the period 1 May 2017 to 30 April 2020. The red line represents the v TEC monthly running average, while the green curve is the 12-month smoothed relative sunspot number R12. The v TEC monthly running average peaks in May (year 2017) and early June (years 2018 and 2019) and presents a decay at such peaks of about 1 TECu per year, that is due to the decrease of the solar flux during the descending phase of the 24th solar cycle, visible as a decreasing R12.

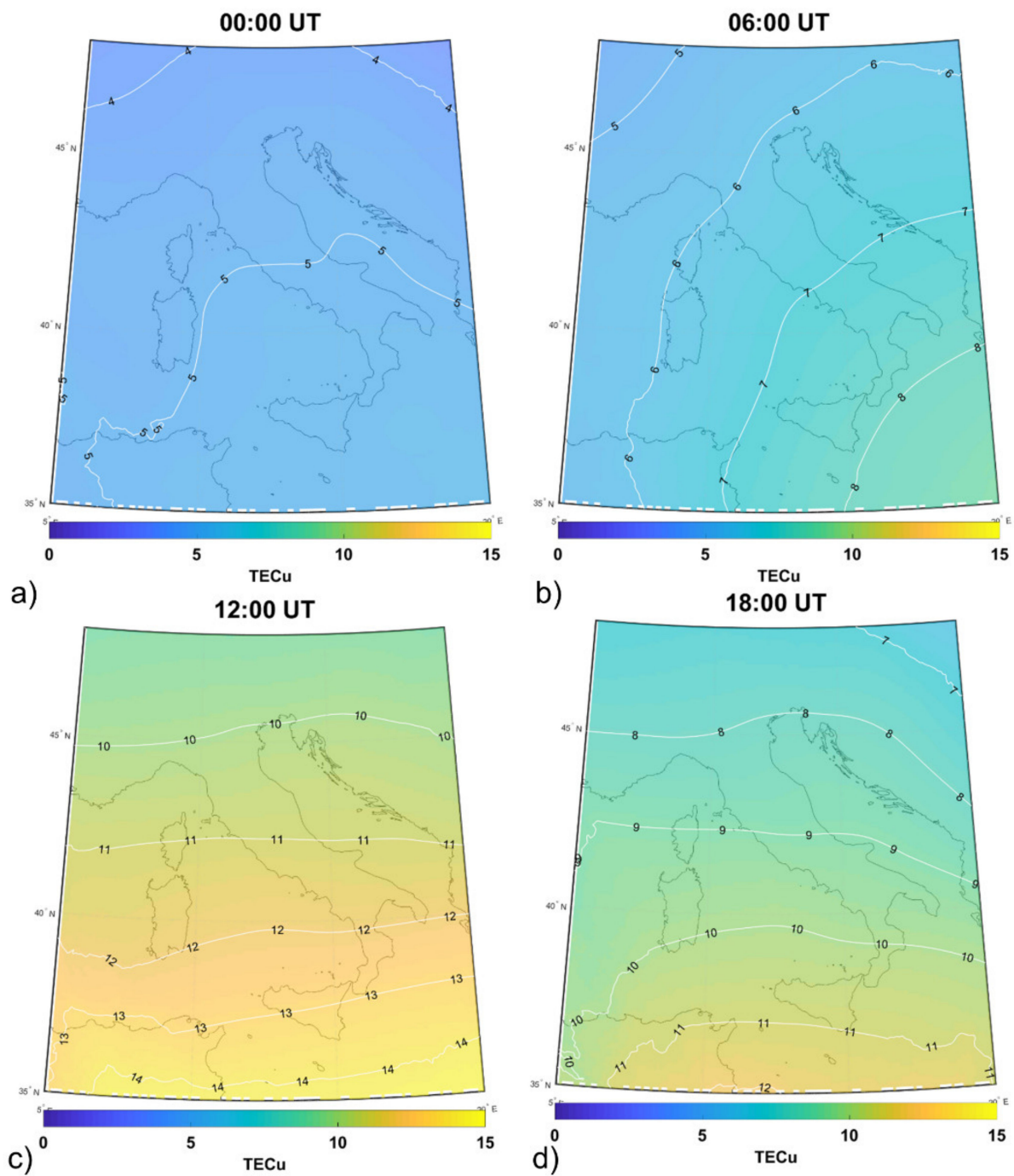


Figure 7. Maps of mean TEC at 00:00 UT (panel a), 06:00 UT (panel b), 12:00 UT (panel c) and 18:00 UT (panel d) by considering the period 1 May 2017 to 30 April 2020.

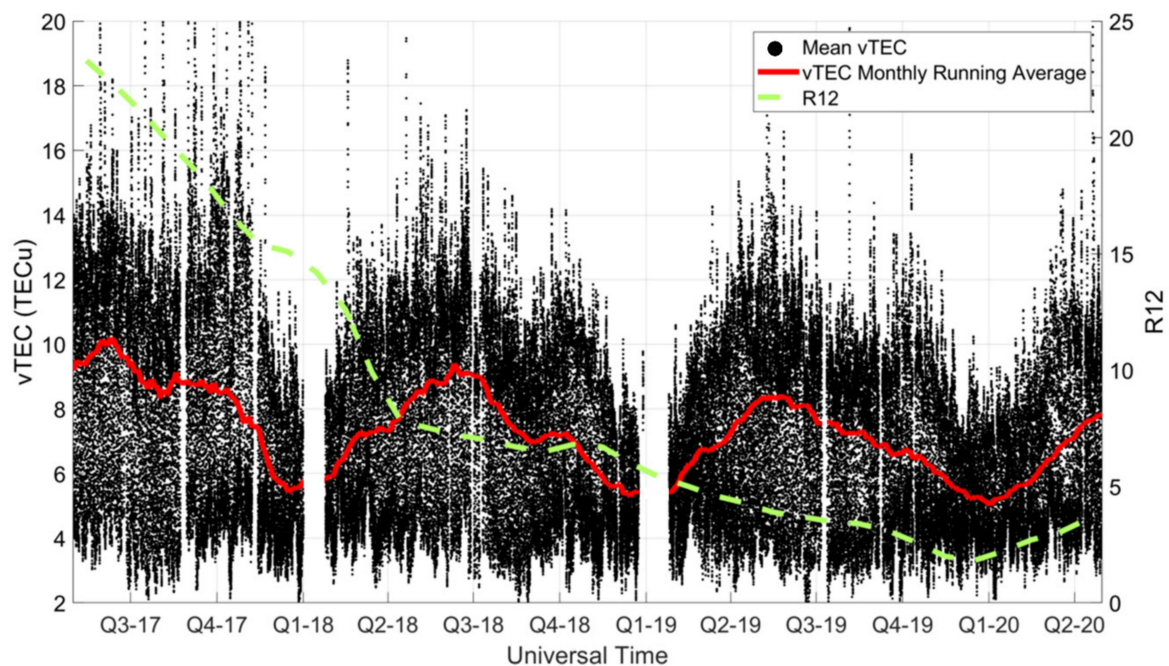


Figure 8. Seasonal variation of mean TEC by considering the period 1 May 2017 to 30 April 2020. Red line represents the TEC monthly running average. Green curve is the 12-months smoothed relative sunspot number R12.

4.2. September 2017 Geomagnetic Storm

The geomagnetic storm that occurred in September 2017 is one of the most investigated of the 24th solar cycle (see e.g., [48–53]) and was featured by the strongest flare event in a decade. It started on 6 September 2017 at 11:53 UT, peaked at 12:02 UT, and was classified as an X9.3. Solar irradiance increases rapidly during solar flare events, peaking within ~10–30 min, and creating abrupt increases of the ionization in the upper atmosphere [Qian et al., 2019]. The occurrence around UT noon enables to study the TEC response over Italy to such a flare, as, at that UT time, it is located close to the subsolar point (6.48°N, 0.41°E), at which the largest TEC gradients driven by solar EUV flux enhancements are expected to take place (see, e.g., [49,53,54]). Within this scope, the top panel of Figure 9 reports the mean value of TEC over Italy for the period 6 September 2017 to 9 September 2017 (red line) and the 27-days (before the X9.3 flare occurrence) running median of mean TEC over Italy (gray dashed line). The mean TEC is calculated by averaging the values over the whole map. The bottom panel of the same figure reports the difference between actual and median TEC (the curves in the top panel, black line) and the disturbance storm time (Dst) index (green line). Blue dashed lines in both panels indicate the starting time of the X9.3 flare. We remind the reader that the TEC-related values in Figure 9 are provided with a 10-minutes cadence. Right after the arrival of the X9.3 flare, a sudden average TEC increase is recorded, passing from 13.6 TECu at 12:00 UT to 15.7 TECu at 12:10 UT, and then it reaches 16.2 TECu at 12:20 UT. Starting from 7 September, two geomagnetic storms occurred (Qian et al., 2019) related to the arrival of Coronal Mass Ejections associated with the X9.3 flare. The Dst index characterizes the geomagnetic storms, with the first and large commencing ~20UT on 7th September and the second storm commencing ~10UT on 8th September. The ionospheric response over Italy is featured by a typical response of the mid-latitude ionosphere [45]. Specifically, there are positive ionospheric conditions after the flare EUV enhancement on the 6th, with a large daytime enhancement on the 7th before the geomagnetic storms. This may be caused by the transport of ionization at F2 heights into the region as a result of the initial ionospheric disturbance from the flare. The initial geomagnetic storm occurs during the local night and does not cause a TEC enhancement, but the second smaller storm in the following morning of the 8th causes

a daytime enhancement positive phase ionospheric storm, though interestingly smaller than that of the 7th before the onset of the geomagnetic storms. Enhanced TEC lasts until ~18:00 UT on the 8th and are followed by a negative phase ionospheric disturbance that is maintained until at least 00:00 UT on the 10th, at the end of the period in Figure 9.

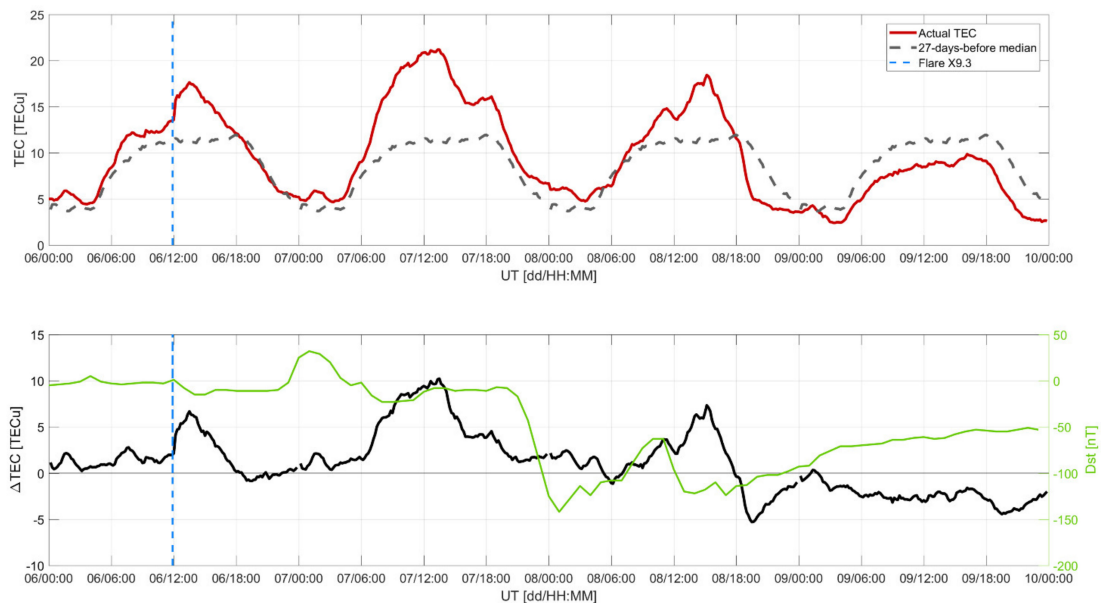


Figure 9. (Top panel) Mean TEC over Italy for the period 6 September 2017 to 9 September 2017 (red line) and 27-days running median (before the X9.3 flare occurrence) of the mean TEC over Italy (gray dashed line). (Bottom panel) Difference between actual and median TEC (reported on top panel, black line) and Dst (green line). Blue dashed line indicates the time of the X9.3 flare peak.

To further characterize the TEC features depicted by IONORING under effective flaring activity, Figure 10 shows the maps for the times between 11:50 UT and 12:30 UT on 6 September 2017. Panels b and c report the maps right before and right after the arrival of the X9.3 flare. The effect of the flare is an increase in TEC all over the considered area. Highlighting the latitudinal dependence of the flare-induced TEC increase, Figure 11 reports the maps ($\Delta\text{TEC}_{\text{median}}$) of the percentage difference between median $v\text{TEC}$ considering 27 days before the X9.3 flare on 6 September 2017 and $v\text{TEC}$ maps at 12:00 UT (panel a), i.e., before the flare, and 12:10 UT (panel b), i.e., after the flare, and the difference $\Delta\text{TEC}_{\text{flare}} = \Delta\text{TEC}_{\text{median}}|_{12:10} - \Delta\text{TEC}_{\text{median}}|_{12:00}$ (panel c). By subtracting $\Delta\text{TEC}_{\text{median}}|_{12:00}$, we are removing the deviation from the median behavior due to effects not related to the flare. Such effects are assumed to be constant between 12:00 UT and 12:10 UT, in agreement with what was reported by Cesaroni et al., 2015 [38] for low-latitude ionosphere, which is featured by larger temporal TEC gradients with respect to mid-latitude ones. Hence, $\Delta\text{TEC}_{\text{flare}}$ represents the flare net effect measured as a percentage of extra ionization. In Figure 11c, $\Delta\text{TEC}_{\text{flare}}$ values are of the order of 20% in the mid- and low latitudes, while of about 10% in the northernmost part of the map. This is reasonably due to a twofold effect. First, the dependence of the flare effects on the distance from the subsolar point (see, e.g., [54]). In addition, from the bottom panel of Figure 9, the flare-induced extra ionization lasts for about 4 h, in agreement with what was reported for the Halloween and Bastille Day storms by Tsurutani et al., 2005 [54]. Such duration is compatible with the hypothesis that the extra ionization is mainly due to the EUV effect on the atomic oxygen in the ionospheric F2 layer, which recombines with a time scale of hours [54]. The atomic oxygen concentration decreases with the latitude, likely resulting in the meridional TEC enhancement distribution shown in Figure 11c. Deviations from this behavior are found in the easternmost part of the map in Figure 11c, where a quiet uniform increase of 20% is present. This is likely due to border effects introduced by the interpolation technique

and by the different local times between maps in Figure 11a,b, from which $\Delta\text{TEC}_{\text{flare}}$ is calculated, which affect the photoionization in the easternmost part.

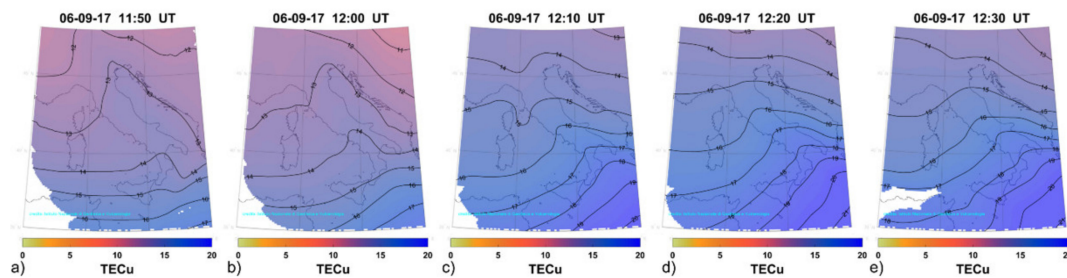


Figure 10. TEC maps for the times between 11:50 UT (panel a), 12:00 UT (panel b), 12:10 UT (panel c), 12:20 UT (panel d) and 12:30 UT (panel e) for 6 September 2017, during which the X9.3 flare occurred.

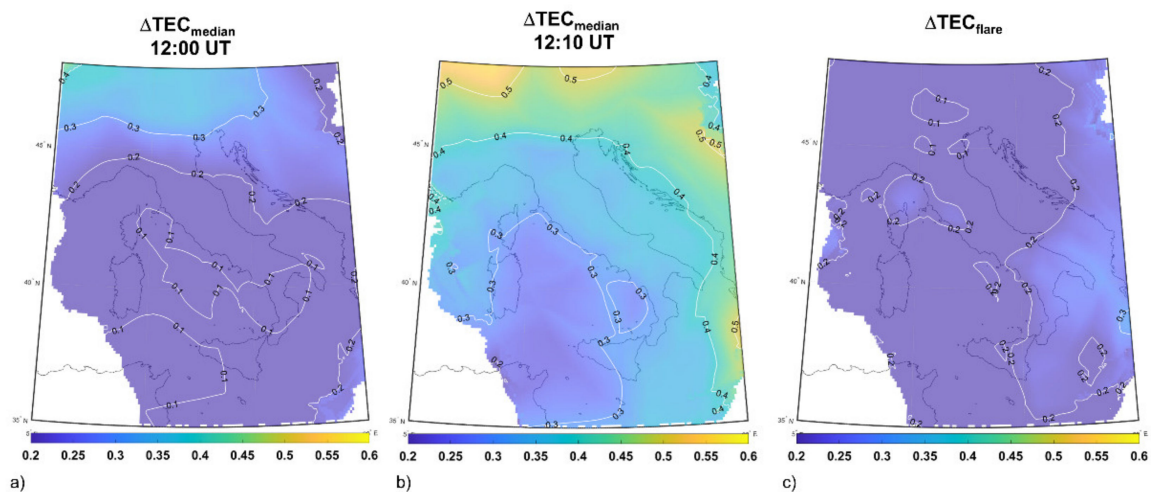


Figure 11. Maps of percentage difference between median $v\text{TEC}$ considering 27-days before the X9.3 flare on 6 September 2017 and $v\text{TEC}$ maps ($\Delta\text{TEC}_{\text{median}}$) at 12:00 UT (panel a), i.e., before the flare, and 12:10 UT (panel b), i.e., after the flare, and the difference between the two ($\Delta\text{TEC}_{\text{flare}}$, panel c).

4.3. Application on Positioning

As an example of application, we test the use of IONORING maps in single-frequency positioning. To the scope, we perform Single Point Positioning (SPP) [55], exploiting the data acquired by the *ingr* receiver (41.83°N, 12.51°E, yellow dot in Figure 1) and processing them in kinematic mode. We remind the reader again that the *ingr* receiver is not included in IONORING. IONORING-based positioning is compared with the ones obtained by using, as ionospheric information, the Klobuchar model [53] and the IGS GIM final combined solution product [17]. It is worth mentioning that this positioning exercise is performed in order to show a possible application of IONORING products and not for validation purposes in the positioning domain that will be the focus of a companion paper. In fact, validation in the positioning domain requires particular attention in not mixing ionospheric induced errors with the ones introduced by other factors, such as clock and orbit errors, measurement noise, pseudo-range multipath, evaluation metric, and outlier's contributions [56]. For this reason, validation on the positioning domain is usually performed by applying the Precise Point Positioning technique that is able to mitigate some of the errors mentioned above by considering precise orbit and clock information. In this paper, positioning results are obtained by running *gLAB* software [57], a tool suite developed under a European Space Agency (ESA) Contract by the research

group of Astronomy and Geomatics (gAGE) from the Universitat Politècnica de Catalunya (UPC) to process and analyze GNSS data.

To the scope, carrier-smoothing of code pseudo-ranges are used, locations of the satellites are calculated by finding the optimal broadcasting ephemeris according to the observing epoch, satellite clock error is calculated by the broadcasting clock error parameters, tropospheric delay correction is calculated using the University of New Brunswick (UNB) model [58], and relativity correction and earth rotation correction are also calculated with models. We perform the positioning under quiet and disturbed ionospheric conditions. As a disturbed day, we select 6 September 2017, being featured by the already discussed X9.3 flare. As a quiet day, we select 25 September 2017, which is suggested in Alfonsi et al., 2021 [48] as suitable to characterize the quiet ionospheric behavior, being featured by quiet geomagnetic conditions, low auroral activity, and seasonal and solar flux conditions similar to those under which the X9.3 flare occurred. Figure 12 shows results of positioning during 25 September 2017 (panel a) and 6 September 2017 (panel b). Both panels report the position of *ingr* calculated by applying SPP technique fed by Klobuchar model (black dots), GIM (blue dots), IONORING (pale yellow dots), and as estimated by Precise Point Positioning (PPP) in static mode (red star), assumed to be the true position. To evaluate the accuracy of the positioning when the different ionospheric corrections are used, Table 2 summarizes the North, East, and Horizontal Position Error (HPE) and the improvement ratio (IR) with respect to the use of the Klobuchar model, which we define as:

$$IR_{GIM,IONORING} = 100 \cdot \frac{HPE_{Klob}^2 - HPE_{GIM,IONORING}^2}{HPE_{Klob}^2} \quad (13)$$

Table 2. Summary table of the positioning results reporting the RMSE of the SPP with respect to the true position (PPP static) and the improvement ratio with respect to the Klobuchar model.

Date	KLOBUCHAR			GIM			IR	IONORING			IR
	North (m)	East (m)	HPE (m)	North (m)	East (m)	HPE (m)		North (m)	East (m)	HPE (m)	
25 Sep 2017	1.25	1.29	3.23	0.51	0.85	0.98	91%	0.76	1.49	2.8	25%
6 Sep 2017	1.04	1.79	4.29	0.9	1.74	3.84	20%	0.75	1.38	2.47	67%

The HPE is of the order of meters in all the cases, but the improvement ratio reveals an increase of the accuracy on the horizontal position of 25% (91%) and 67% (25%) when using IONORING (GIM) during quiet and disturbed days, respectively. We remind the reader that GIM are available with a latency of about 11 days, while IONORING is a real-time product, so, despite the fact that GIMs perform better than IONORING in quiet conditions, IONORING is a valuable added value in real-time positioning applications. During disturbed conditions, IONORING seems to perform better than Klobuchar and GIM.

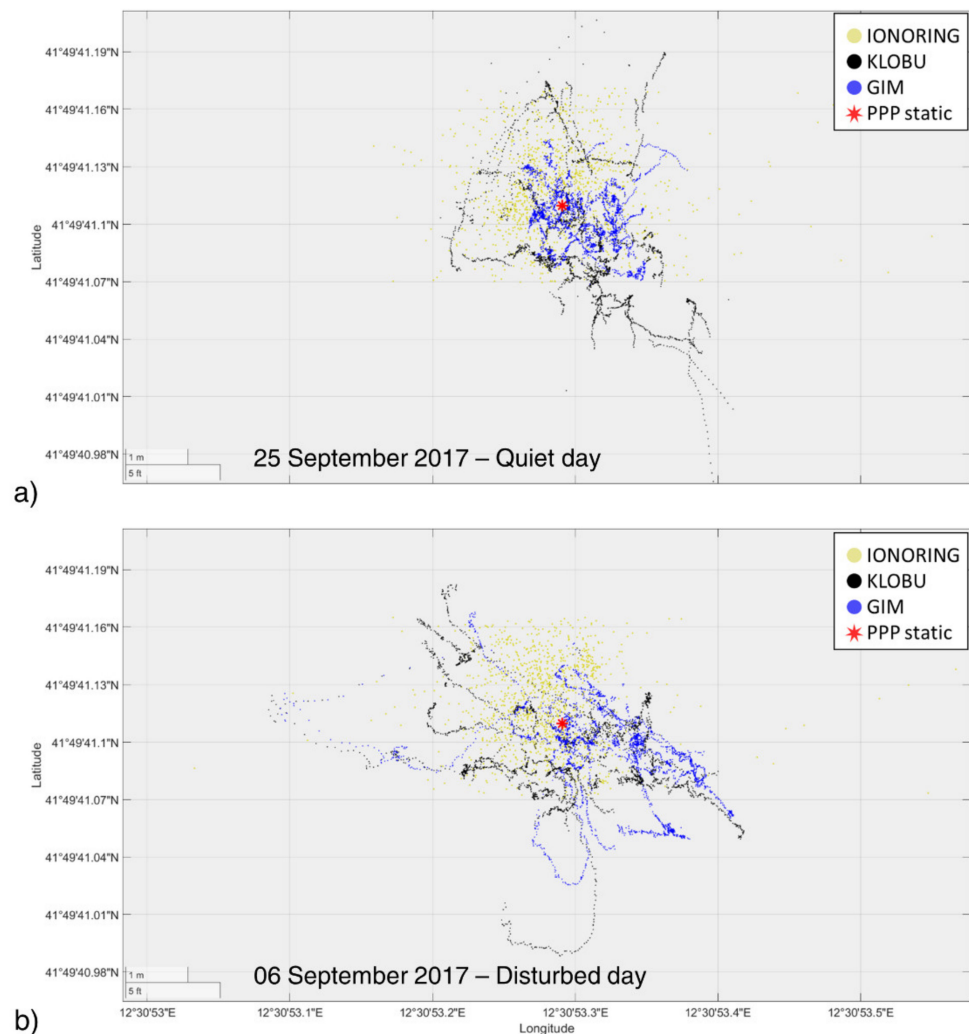


Figure 12. Single point positioning considering one quiet (25 September 2017, panel **a**) and one disturbed (6 September 2017, panel **b**) day of data from the ingr receiver realized by using different ionospheric information: IONORING TEC maps (pale yellow), Klobuchar model (black), and IGS GIMs (blue). The red star indicates the ground truth estimated with PPP in static mode.

5. Conclusions

In this paper, we present IONORING: a real-time tool for ionospheric monitoring and modeling over Italy. IONORING exploits the data provided by the RING network managed by INGV, which has been conceived for geodetic purposes. IONORING provides maps of vertical TEC with a cadence of 10 min, a spatial resolution of 0.1° latitude \times 0.1° longitude, and a latency of less than a minute. The reliability of IONORING has been proved by comparing the vTEC maps produced over a 3-year period (May 2017–April 2020) with independent vTEC measurements (Gg calibration technique, ROB vTEC maps, and GIM). Such comparison has shown a very good accuracy of IONORING products being the RMSEs equal to 1.2 TECu, 2.0 TECu, and 2.9 TECu for Gg vTEC, ROB, and IGS final combined maps, respectively.

In addition, IONORING capability to depict the seasonal, daily, and latitudinal variations as well as the dependence on the solar activity and to depict the ionospheric response to the September 2017 geomagnetic storm has been shown.

The daily variation of mean vTEC reveals a peak of 9.6 ± 0.8 TECu at 11:00 UT (12:00 LT) for higher latitudes and a peak of 14.6 ± 1.6 TECu for lower latitudes at later times, i.e., 13:00 UT (14:00 LT). This highlights the influence of the northern crest of the

EIA on vTEC at Italian lower latitudes. The monthly running average of vTEC between May 2017 and April 2020 reproduces the expected seasonal variation (maximizing vTEC in May/June) and presents a decay of about 1 TECu per year, matching the behavior of the solar activity.

The storm-time behavior is also well depicted by IONORING. Specifically, the positive and negative phases of the geomagnetic storm that occurred in September 2017 and the effect of the X9.3 flare that started at 11:53 UT on 6 September are well characterized. In particular, the mean vTEC enhancement over Italy induced by the flare is 2.6 TECu at 12:20 UT, resulting in a net TEC increase ranging between 10% (higher latitudes) and 20% (lower latitudes).

As an example of application, IONORING has been tested as external ionospheric information single frequency standard point positioning showing an improvement in the performance in terms of horizontal error of 25% (91%) and 67% (25%) when using IONORING (GIM) during a quiet and disturbed day, respectively. Despite having been tested on a single day, there is a promising indication that IONORING performs better than the GIM final product under disturbed conditions. Under quiet conditions, IONORING presents a smaller improvement ratio than the GIM final product. However, the latter cannot be used in real-time, likely indicating that IONORING provides a valuable added value in real-time positioning applications. Such features are currently under investigation for further assessments on larger statistics and against also IGS rapid products, for real-time positioning purposes.

Proven such capabilities, IONORING is a precious tool to support either research and services. In the recent past, it has been used to characterize the ionospheric effect of a moderate storm in the mid-low latitude boundary region [12]. Moreover, it is one of the algorithms currently running in the Ionospheric Prediction Service (IPS, <https://ionospheric-prediction.jrc.ec.europa.eu>, accessed on 13 July 2021) [59] as a now-casting product and as input to a tool dedicated to the detection and estimation of the main characteristics of Medium-Scale Traveling Ionospheric Disturbances (MSTIDs). Additionally, the maps from IONORING are part of the product portfolio of the PECASUS consortium (<http://pecasus.eu/>, accessed on 13 July 2021), that is one of the three global centers providing space weather advisories according to International Civil Aviation Organization (ICAO) regulations.

IONORING output (Upper atmosphere physics and radio propagation Working Group et al., 2020) is available as images and JSON files through eSWua web portal (eswua.ingv.it) [60]. These can be downloaded by using the download tools (<http://eswua.ingv.it/index.php/data-access-and-policy/download-tools>, accessed on 13 July 2021) or via the dedicated web service (<http://eswua.ingv.it/index.php/data-access-and-policy/web-service>, accessed on 13 July 2021).

Author Contributions: Conceptualization, all authors; methodology, C.C. and L.S.; software, C.C. and L.S.; validation, C.C. and L.S.; data curation, C.C.; writing—original draft preparation, L.S. and G.D.F.; writing—review and editing, all authors. All authors have read and agreed to the published version of the manuscript.

Funding: This research is part of “Progetto INGV Pianeta Dinamico (Codice Unico Progetto: CUP D53J19000170001) funded by MUR (“Fondo finalizzato al rilancio degli investimenti delle amministrazioni centrali dello Stato e allo sviluppo del Paese, legge 145/2018”), Tema 8–ATTEMPT–2021.

Institutional Review Board Statement: Not applicable.

Informed Consent Statement: Not applicable.

Data Availability Statement: The data presented in this study are openly available in eSWua web-portal at <https://doi.org/10.13127/eswua/tec>, accessed on 13 July 2021.

Acknowledgments: Authors are grateful to Luigi “Gg” Ciralo for the provision of the TEC calibration and the precious discussions about it. Authors also thank Carlo Marcocci and Emanuele Pica for their work for the development of IONORING within eSWua web portal. Authors thank Vincenzo Romano and Lucilla Alfonsi for valuable discussions. RING stations (INGV RING WORKING GROUP (2016), RETE INTEGRATA NAZIONALE GPS, DOI:10.13127/RING) are managed by INGV Earthquake department. Authors thank ROB and IGS for making available the TEC maps used for validation.

Conflicts of Interest: The authors declare no conflict of interest.

References

1. Schrijver, C.J. Socio-Economic Hazards and Impacts of Space Weather: The Important Range between Mild and Extreme. *Space Weather* **2015**, *13*, 524–528. [[CrossRef](#)]
2. De Franceschi, G.; Spogli, L.; Alfonsi, L.; Romano, V.; Cesaroni, C.; Hunstad, I. The ionospheric irregularities climatology over Svalbard from solar cycle 23. *Sci. Rep.* **2019**, *9*, 1–14. [[CrossRef](#)]
3. Spogli, L.; Cesaroni, C.; Di Mauro, D.; Pezzopane, M.; Alfonsi, L.; Musicò, E.; Povero, G.; Pini, M.; Dovis, F.; Romero, R.; et al. Formation of ionospheric irregularities over Southeast Asia during the 2015 St. Patrick’s Day storm. *J. Geophys. Res. Space Phys.* **2016**, *121*, 12,211–12,233. [[CrossRef](#)]
4. Spogli, L.; Sabbagh, D.; Regi, M.; Cesaroni, C.; Perrone, L.; Alfonsi, L.; Di Mauro, D.; Lepidi, S.; Campuzano, S.A.; Marchetti, D.; et al. Ionospheric Response Over Brazil to the August 2018 Geomagnetic Storm as Probed by CSES-01 and Swarm Satellites and by Local Ground-Based Observations. *J. Geophys. Res. Space Phys.* **2021**, *126*. [[CrossRef](#)]
5. Mannucci, A.J.; Tsurutani, B.T.; Iijima, B.A.; Komjathy, A.; Saito, A.; Gonzalez, W.D.; Guarnieri, F.L.; Kozyra, J.U.; Skoug, R. Dayside global ionospheric response to the major interplanetary events of 29–30 October 2003 “Halloween Storms”. *Geophys. Res. Lett.* **2005**, *32*. [[CrossRef](#)]
6. Yang, Z.; Mrak, S.; Morton, Y.J. Geomagnetic Storm Induced Mid-latitude Ionospheric Plasma Irregularities and Their Implications for GPS Positioning over North America: A Case Study. In Proceedings of the 2020 IEEE/ION Position, Location and Navigation Symposium (PLANS), Portland, OR, USA, 20–23 April 2020; pp. 234–238. [[CrossRef](#)]
7. Ledvina, B.M.; Makela, J.; Kintner, P.M. First observations of intense GPS L1 amplitude scintillations at midlatitude. *Geophys. Res. Lett.* **2002**, *29*, 4-1–4-4. [[CrossRef](#)]
8. Balan, N.; Liu, L.; Le, H. A brief review of equatorial ionization anomaly and ionospheric irregularities. *Earth Planet. Phys.* **2018**, *2*, 1–19. [[CrossRef](#)]
9. Li, G.; Ning, B.; Otsuka, Y.; Abdu, M.A.; Abadi, P.; Liu, Z.; Spogli, L.; Wan, W. Challenges to Equatorial Plasma Bubble and Ionospheric Scintillation Short-Term Forecasting and Future Aspects in East and Southeast Asia. *Surv. Geophys.* **2020**, *42*, 201–238. [[CrossRef](#)]
10. Shiokawa, K.; Otsuka, Y.; Ogawa, T.; Balan, N.; Igarashi, K.; Ridley, A.; Knipp, D.; Saito, A.; Yumoto, K. A large-scale traveling ionospheric disturbance during the magnetic storm of 15 September 1999. *J. Geophys. Res. Space Phys.* **2002**, *107*, SIA 5-1–SIA 5-11. [[CrossRef](#)]
11. Zakharenkova, I.; Astafyeva, E.; Cherniak, I. GPS and GLONASS observations of large-scale traveling ionospheric disturbances during the 2015 St. Patrick’s Day storm. *J. Geophys. Res. Space Phys.* **2016**, *121*, 12,138–12,156. [[CrossRef](#)]
12. Cesaroni, C.; Alfonsi, L.; Pezzopane, M.; Martinis, C.; Baumgardner, J.; Wroten, J.; Mendillo, M.; Musicò, E.; Lazzarin, M.; Umbriaco, G. The First Use of Coordinated Ionospheric Radio and Optical Observations Over Italy: Convergence of High- and Low-Latitude Storm-Induced Effects. *J. Geophys. Res. Space Phys.* **2017**, *122*, 11,794–11,806. [[CrossRef](#)]
13. Park, J.; Sreeja, V.; Aquino, M.; Cesaroni, C.; Spogli, L.; Dodson, A.; De Franceschi, G. Performance of ionospheric maps in support of long baseline GNSS kinematic positioning at low latitudes. *Radio Sci.* **2016**, *51*, 429–442. [[CrossRef](#)]
14. Klobuchar, J.A. Ionospheric Time-Delay Algorithm for Single-Frequency GPS Users. *IEEE Trans. Aerosp. Electron. Syst.* **1987**, *AES-23*, 325–331. [[CrossRef](#)]
15. Yuan, Y.; Wang, N.; Li, Z.; Huo, X. The BeiDou global broadcast ionospheric delay correction model (BDGIM) and its preliminary performance evaluation results. *NAVIGATION* **2019**, *66*, 55–69. [[CrossRef](#)]
16. Yuan, Y.; Ou, J. Auto-covariance estimation of variable samples (ACEVS) and its application for monitoring random ionospheric disturbances using GPS. *J. Geod.* **2001**, *75*, 438–447. [[CrossRef](#)]
17. Hernández-Pajares, M.; Juan, J.M.; Sanz, J.; Orus, R.; García-Rigo, A.; Feltens, J.; Komjathy, A.; Schaer, S.C.; Krankowski, A. The IGS VTEC maps: A reliable source of ionospheric information since 1998. *J. Geod.* **2009**, *83*, 263–275. [[CrossRef](#)]
18. Hernández-Pajares, M.; Roma-Dollase, D.; Krankowski, A.; García-Rigo, A.; Orús-Pérez, R. Methodology and consistency of slant and vertical assessments for ionospheric electron content models. *J. Geod.* **2017**, *91*, 1405–1414. [[CrossRef](#)]
19. Li, Z.; Wang, N.; Hernández-Pajares, M.; Yuan, Y.; Krankowski, A.; Liu, A.; Zha, J.; García-Rigo, A.; Roma-Dollase, D.; Yang, H.; et al. IGS real-time service for global ionospheric total electron content modeling. *J. Geod.* **2020**, *94*, 1–16. [[CrossRef](#)]
20. Reinisch, B.W.; Galkin, I.A. Global Ionospheric Radio Observatory (GIRO). *Earth Planets Space* **2011**, *63*, 377–381. [[CrossRef](#)]

21. Bilitza, D.; Altadill, D.; Truhlik, V.; Shubin, V.; Galkin, I.; Reinisch, B.; Huang, X. International Reference Ionosphere 2016: From ionospheric climate to real-time weather predictions. *Space Weather* **2017**, *15*, 418–429. [[CrossRef](#)]
22. Froñ, A.; Galkin, I.; Krankowski, A.; Bilitza, D.; Hernández-Pajares, M.; Reinisch, B.; Li, Z.; Kotulak, K.; Zakharenkova, I.; Cherniak, I.; et al. Towards Cooperative Global Mapping of the Ionosphere: Fusion Feasibility for IGS and IRI with Global Climate VTEC Maps. *Remote Sens.* **2020**, *12*, 3531. [[CrossRef](#)]
23. Bergeot, N.; Chevalier, J.-M.; Bruyninx, C.; Pottiaux, E.; Aerts, W.; Baire, Q.; Legrand, J.; Defraigne, P.; Huang, W. Near real-time ionospheric monitoring over Europe at the Royal Observatory of Belgium using GNSS data. *J. Space Weather. Space Clim.* **2014**, *4*, A31. [[CrossRef](#)]
24. Aa, E.; Huang, W.; Yu, S.; Liu, S.; Shi, L.; Gong, J.; Chen, Y.; Shen, H. A regional ionospheric TEC mapping technique over China and adjacent areas on the basis of data assimilation. *J. Geophys. Res. Space Phys.* **2015**, *120*, 5049–5061. [[CrossRef](#)]
25. Mendoza, L.P.O.; Meza, A.M.; Paz, J.M.A. A Multi-GNSS, Multifrequency, and Near-Real-Time Ionospheric TEC Monitoring System for South America. *Space Weather* **2019**, *17*, 654–661. [[CrossRef](#)]
26. Opperman, B.D.; Cilliers, P.J.; McKinnell, L.-A.; Haggard, R. Development of a regional GPS-based ionospheric TEC model for South Africa. *Adv. Space Res.* **2007**, *39*, 808–815. [[CrossRef](#)]
27. De Santis, A.; de Franceschi, G.; Zolesi, B.; Pau, S.; Cander, L.R. Regional Mapping of the Critical Frequency of the F2 Layer by Spherical Cap Harmonic Expansion. *AnGeo* **1991**, *9*, 401–406.
28. De Franceschi, G.; De Santis, A.; Pau, S. Ionospheric mapping by regional spherical harmonic analysis: New developments. *Adv. Space Res.* **1994**, *14*, 61–64. [[CrossRef](#)]
29. Li, W.; Zhao, D.; Shen, Y.; Zhang, K. Modeling Australian TEC Maps Using Long-Term Observations of Australian Regional GPS Network by Artificial Neural Network-Aided Spherical Cap Harmonic Analysis Approach. *Remote Sens.* **2020**, *12*, 3851. [[CrossRef](#)]
30. Musico, E.; Cesaroni, C.; Spogli, L.; Boncori, J.P.M.; De Franceschi, G.; Seu, R. The Total Electron Content from InSAR and GNSS: A Midlatitude Study. *IEEE J. Sel. Top. Appl. Earth Obs. Remote Sens.* **2018**, *11*, 1725–1733. [[CrossRef](#)]
31. Tornatore, V.; Cesaroni, C.; Pezzopane, M.; Alizadeh, M.; Schuh, H. Performance Evaluation of VTEC GIMs for Regional Applications during Different Solar Activity Periods, Using RING TEC Values. *Remote Sens.* **2021**, *13*, 1470. [[CrossRef](#)]
32. Ciralo, L.; Azpilicueta, F.; Brunini, C.; Meza, A.; Radicella, S.M. Calibration errors on experimental slant total electron content (TEC) determined with GPS. *J. Geod.* **2006**, *81*, 111–120. [[CrossRef](#)]
33. Pi, X.; Mannucci, A.J.; Lindqwister, U.J.; Ho, C.M. Monitoring of global ionospheric irregularities using the Worldwide GPS Network. *Geophys. Res. Lett.* **1997**, *24*, 2283–2286. [[CrossRef](#)]
34. Mannucci, A.J.; Wilson, B.D.; Yuan, D.N.; Ho, C.H.; Lindqwister, U.J.; Runge, T.F. A global mapping technique for GPS-derived ionospheric total electron content measurements. *Radio Sci.* **1998**, *33*, 565–582. [[CrossRef](#)]
35. Rawer, K.; Kouris, S.; Fotiadis, D. Variability of F2 parameters depending on MODIP. *Adv. Space Res.* **2003**, *31*, 537–541. [[CrossRef](#)]
36. Brunini, C.; Azpilicueta, F. GPS slant total electron content accuracy using the single layer model under different geomagnetic regions and ionospheric conditions. *J. Geod.* **2010**, *84*, 293–304. [[CrossRef](#)]
37. Piersanti, M.; Cesaroni, C.; Spogli, L.; Alberti, T. Does TEC react to a sudden impulse as a whole? The 2015 Saint Patrick's day storm event. *Adv. Space Res.* **2017**, *60*, 1807–1816. [[CrossRef](#)]
38. Cesaroni, C.; Spogli, L.; Alfonsi, L.; De Franceschi, G.; Ciralo, L.; Monico, J.F.G.; Scotto, C.; Romano, V.; Aquino, M.; Bougard, B. L-band scintillations and calibrated total electron content gradients over Brazil during the last solar maximum. *J. Space Weather Space Clim.* **2015**, *5*, A36. [[CrossRef](#)]
39. Olwendo, O.; Cesaroni, C. Validation of NeQuick 2 model over the Kenyan region through data ingestion and the model application in ionospheric studies. *J. Atmos. Solar-Terr. Phys.* **2016**, *145*, 143–153. [[CrossRef](#)]
40. Olwendo, O.; Cesaroni, C.; Yamazaki, Y.; Cilliers, P. Equatorial ionospheric disturbances over the East African sector during the 2015 St. Patrick's day storm. *Adv. Space Res.* **2017**, *60*, 1817–1826. [[CrossRef](#)]
41. Pezzopane, M.; Del Corpo, A.; Piersanti, M.; Cesaroni, C.; Pignalberi, A.; Di Matteo, S.; Spogli, L.; Vellante, M.; Heilig, B. On some features characterizing the plasmasphere–magnetosphere–ionosphere system during the geomagnetic storm of 27 May 2017. *Earth Planets Space* **2019**, *71*, 1–21. [[CrossRef](#)]
42. Sardón, E.; Zarraoa, N. Estimation of total electron content using GPS data: How stable are the differential satellite and receiver instrumental biases? *Radio Sci.* **1997**, *32*, 1899–1910. [[CrossRef](#)]
43. Cleveland, W.S. Robust Locally Weighted Regression and Smoothing Scatterplots. *J. Am. Stat. Assoc.* **1979**, *74*, 829–836. [[CrossRef](#)]
44. Hargreaves, J. *The Solar-Terrestrial Environment*; Cambridge University Press: Cambridge, UK, 1992.
45. Mendillo, M. Storms in the ionosphere: Patterns and processes for total electron content. *Rev. Geophys.* **2006**, *44*. [[CrossRef](#)]
46. Roble, R. The calculated and observed diurnal variation of the ionosphere over Millstone Hill on 23–24 March 1970. *Planet. Space Sci.* **1975**, *23*, 1017–1033. [[CrossRef](#)]
47. Xiong, C.; Lühr, H.; Ma, S. The magnitude and inter-hemispheric asymmetry of equatorial ionization anomaly-based on CHAMP and GRACE observations. *J. Atmos. Solar-Terr. Phys.* **2013**, *105-106*, 160–169. [[CrossRef](#)]
48. Alfonsi, L.; Cesaroni, C.; Spogli, L.; Regi, M.; Paul, A.; Ray, S.; Lepidi, S.; Di Mauro, D.; Haralambous, H.; Oikonomou, C.; et al. Ionospheric Disturbances Over the Indian Sector During 8 September 2017 Geomagnetic Storm: Plasma Structuring and Propagation. *Space Weather* **2021**, *19*, e2020SW002607. [[CrossRef](#)]

49. Berdermann, J.; Kriegel, M.; Banyś, D.; Heymann, F.; Hoque, M.M.; Wilken, V.; Borries, C.; Hesselbarth, A.; Jakowski, N. Ionospheric Response to the X9.3 Flare on 6 September 2017 and Its Implication for Navigation Services Over Europe. *Space Weather* **2018**, *16*, 1604–1615. [[CrossRef](#)]
50. Sato, H.; Jakowski, N.; Berdermann, J.; Jiricka, K.; Heßelbarth, A.; Banyś, D.; Wilken, V. Solar Radio Burst Events on 6 September 2017 and Its Impact on GNSS Signal Frequencies. *Space Weather*. **2019**, *17*, 816–826. [[CrossRef](#)]
51. De Castro, C.G.G.; Raulin, J.; Silva, J.F.V.; Simões, P.J.A.; Kudaka, A.S.; Valio, A. The 6 September 2017 X9 Super Flare Observed From Submillimeter to Mid-IR. *Space Weather*. **2018**, *16*, 1261–1268. [[CrossRef](#)]
52. Linty, N.; Minetto, A.; Dovis, F.; Spogli, L. Effects of Phase Scintillation on the GNSS Positioning Error During the September 2017 Storm at Svalbard. *Space Weather*. **2018**, *16*, 1317–1329. [[CrossRef](#)]
53. Qian, L.; Wang, W.; Burns, A.G.; Chamberlin, P.C.; Coster, A.; Zhang, S.; Solomon, S.C. Solar Flare and Geomagnetic Storm Effects on the Thermosphere and Ionosphere During 6–11 September 2017. *J. Geophys. Res. Space Phys.* **2019**, *124*, 2298–2311. [[CrossRef](#)]
54. Tsurutani, B.T.; Judge, D.L.; Guarnieri, F.L.; Gangopadhyay, P.; Jones, A.R.; Nuttall, J.; Zambon, G.A.; Didkovsky, L.; Mannucci, A.J.; Iijima, B.; et al. The October 28, 2003 extreme EUV solar flare and resultant extreme ionospheric effects: Comparison to other Halloween events and the Bastille Day event. *Geophys. Res. Lett.* **2005**, *32*. [[CrossRef](#)]
55. Wu, X.; Hu, X.; Wang, G.; Zhong, H.; Tang, C. Evaluation of COMPASS ionospheric model in GNSS positioning. *Adv. Space Res.* **2013**, *51*, 959–968. [[CrossRef](#)]
56. Rovira-Garcia, A.; Ibáñez-Segura, D.; Orús-Perez, R.; Juan, J.M.; Sanz, J.; González-Casado, G. Assessing the quality of ionospheric models through GNSS positioning error: Methodology and results. *GPS Solutions* **2019**, *24*, 1–12. [[CrossRef](#)]
57. Segura, D.I.; Garcia, A.R.; Alonso, M.T.; Sanz, J.; Juan, J.M.; Casado, G.G.; Martínez, M.L. EGNOS 1046 Maritime Service Assessment. *Sensors* **2020**, *20*, 276. [[CrossRef](#)]
58. Leandro, R.; Santos, M.; Langley, R. UNB Neutral Atmosphere Models: Development and Performance. In Proceedings of the 2006 National Technical Meeting of The Institute of Navigation, Monterey, CA, USA, 18–20 January 2006; pp. 564–573.
59. Veetil, S.V.; Cesaroni, C.; Aquino, M.; De Franceschi, G.; Berrili, F.; Rodriguez, F.; Spogli, L.; Del Moro, D.; Cristaldi, A.; Romano, V.; et al. The ionosphere prediction service prototype for GNSS users. *J. Space Weather. Space Clim.* **2019**, *9*, A41. [[CrossRef](#)]
60. Pica, E.; Marcocci, C.; Cesaroni, C.; Zuccheretti, E.; Pezzopane, M.; Vecchi, S.; Romano, V.; Spogli, L.; Pica, E.; Marcocci, C.; et al. *The SWIT-ESWua System: Managing, Preservation and Sharing of the Historical and near Real-Time Ionospheric Data at the INGV. AGUFM 2020*; Earth and Space Science Open Archive ESSOAr: Washington, DC, USA, 2020.